PNAS RESEARCH ARTICLE | MICROBIOLOGY OPEN ACCESS

A broadly conserved gram-positive lipoprotein regulates cell elongation

Anna P. Brogan[a], Ernst W. Schmid[a], and David Z. Rudner[a,1]

Edited by Joe Lutkenhaus, University of Kansas Medical Center, Kansas City, KS; received March 25, 2026; accepted May 21, 2026

The cell wall peptidoglycan (PG) protects virtually all bacteria from osmotic lysis and specifies cell shape. Synthesis of this exoskeleton is carried out by enzymes that polymerize glycan strands and transpeptidases that crosslink them into the existing cell wall matrix. In many bacteria, a broadly conserved cell wall synthesis complex known as the Rod complex or elongasome plays an essential role in cell growth. To investigate whether there are undiscovered Rod complex components, we combined high-throughput genetics with AlphaFold-Multimer screens. The two approaches converged on the lipoprotein ClcR (formerly, YerH or CamS). ClcR is broadly conserved among gram-positive bacteria and is predicted to interact with the Rod complex transpeptidases. We find that ClcR contributes to proper cell wall synthesis in *Bacillus subtilis* and *Staphylococcus aureus* and is essential for proper elongation and cell shape in *Bacillus anthracis*. We show that ClcR orthologs interact with their cognate transpeptidases and function as positive regulators of Rod complex activity in a distinct pathway from that of the known regulators MreCD. Altogether, our data define a broadly conserved component of the cell wall elongation machinery. As part of this study, we built a webtool to facilitate visualization and analysis of transposon-sequencing datasets. Our findings and accompanying resources provide a framework for uncovering biologically relevant protein–protein interactions that pairs genetic and in silico approaches.

peptidoglycan | Rod complex | AlphaFold-Multimer | class B PBP | CamS

Significance

High throughput in silico protein interaction and functional genomic screens are powerful approaches that generate large datasets but it can be difficult to derive mechanistic insights from these data. We show that combining these approaches can reveal biologically relevant protein–protein interactions. Using paired in silico interaction and functional genomic screens, we identified a broadly conserved component of the cell wall synthesis machinery in gram-positive bacteria. This factor (ClcR) is a positive regulator of class B penicillin binding proteins in the Rod complex and is important for peptidoglycan synthesis in *Bacillus subtilis* and *Staphylococcus aureus* and essential for growth in *Bacillus anthracis* .

Virtually all bacteria are encased within an exoskeleton composed of peptidoglycan called the cell wall. The cell wall peptidoglycan (PG) is composed of long glycan strands that are crosslinked together by short peptides (1). This meshwork plays an essential role in resisting cytoplasmic turgor and specifies cell shape. Peptidoglycan synthesis is carried about by two types of glycan strand polymerases: Class A penicillin binding proteins (aPBPs) and Shape Elongation Division and Sporulation (SEDS) polymerases. aPBPs are bifunctional enzymes with glycosyltransferase domains that polymerize the glycan strands and transpeptidase domains that crosslink the nascent strands into the PG meshwork. The SEDS polymerases are a distinct family of glycosyltransferases that function with cognate class B penicillin binding proteins (bPBPs) that are monofunctional transpeptidases. SEDS–bPBP pairs function in larger macromolecular complexes that are essential for cell wall synthesis during division (the divisome) and cell elongation (the elongasome or Rod complex) (1).

Although the enzymes responsible for PG synthesis by the division and elongation machineries have been well defined, their regulation remains incompletely understood. In the rod-shaped model organisms *Escherichia coli* and *Bacillus subtilis*, the roles of the essential members of the core division and elongation complexes in regulating the SEDS–bPBP enzymes have begun to be elucidated. In the Rod complex, the SEDS glycosyltransferase RodA and its cognate bPBP (PBP2 in *E. coli*, PBP2A and PBPH in *B. subtilis*) are regulated by the membrane proteins MreC and MreD (2–8). In response to unknown stimuli, MreC interacts with the hinge region of the bPBP, likely promoting its active state (9, 10). The filament-forming actin homolog MreB serves as a scaffold for the membrane complex and functions as a rudder guiding circumferential synthesis perpendicular to the long axis of the cell (11, 12). *B. subtilis* contains three MreB paralogs: MreB, Mbl, and MreBH, that are largely functionally redundant (13). Finally, recent work in *E. coli* has revealed that the elusive Rod complex component RodZ regulates MreCD via its extracellular linker and MreB via its intracellular juxtamembrane domain (14–16). In turn, RodZ activity is regulated via phosphorylation by the cell wall stress-sensing kinase PrkC (17). These core components of the Rod complex are critical for elongation of all rod-shaped bacteria studied to date. Recent work suggests that nonessential regulators may play additional roles. For example, the *B. subtilis* transmembrane protein RagB has been reported to interact with and stimulate RodA glycosyltransferase activity (18).

Author affiliations: [a]Department of Microbiology, Harvard Medical School, Boston, MA 02115

Author contributions: A.P.B. and D.Z.R. designed research; A.P.B. performed research; A.P.B. and E.W.S. contributed new reagents/analytic tools; A.P.B. and D.Z.R. analyzed data; and A.P.B. and D.Z.R. wrote the paper.

The authors declare no competing interest.

This article is a PNAS Direct Submission.

[1]To whom correspondence may be addressed. Email: rudner@hms.harvard.edu.

This article contains supporting information online at https://www.pnas.org/lookup/suppl/doi:10.1073/pnas.2610431123/-/DCSupplemental.

Published June 23, 2026.

Additionally, the *B. subtilis* TseB protein has been suggested to regulate PBP2A (19).

Although most of the work on Rod complex function and regulation has been performed in *E. coli* and *B. subtilis*, studies in nonmodel organisms have identified novel factors that regulate cell envelope biogenesis during division and elongation (20–30). These studies have also revealed that broadly conserved factors can play major or minor roles in PG synthesis in different species. We therefore reasoned that broadly conserved factors that are nonessential components of the Rod complex in *B. subtilis* could play critical roles in cell wall elongation in other organisms.

To identify undiscovered Rod complex components in *B. subtilis*, we combined genetic and in silico screens. Large-scale AlphaFold-Multimer (AF-M) screens have emerged as a powerful approach to identify novel protein–protein interactions (31–33). However, many of the hits from these screens are false positives or have little to no phenotype when disrupted. We therefore sought to combine this approach with a genetic screen to identify interactors that are likely to be biologically relevant. Accordingly, we performed a Transposon-sequencing (Tn-seq) screen in a strain in which a component of the Rod complex was partially depleted and separately performed one-by-all AF-M screens using each of the core Rod complex components. The two screens converged on a small number of potential Rod complex regulators or cofactors. Our follow up characterization revealed that the lipoprotein YerH (renamed ClcR) is important for cell elongation by the Rod complex in *B. subtilis* and *Staphylococcus aureus* and is essential for elongation in *Bacillus anthracis*. Our data support a model in which ClcR interacts with the bPBP of the Rod complex to positively regulate its activity in a manner that is independent from the regulation by MreC and MreD. Altogether, our study establishes a method to harness AF-M screens to identify biologically relevant protein–protein interactions; defines a broadly conserved Rod complex component; and provides a clear example of a conserved regulator of an essential process that is critical in some organisms but dispensable in others.

Results

Paired Tn-seq and AlphaFold Screens Identify ClcR as a Potential Rod Complex Component. To screen for new genes involved in Rod complex PG synthesis, we generated a sensitized background in which the activity of the complex was limiting. Specifically, we constructed an IPTG-regulated allele of *pbpA*, encoding PBP2A, the major Rod complex bPBP. Depletion of this enzyme in a strain lacking native *pbpA* and the *pbpH* gene, encoding the functionally redundant Rod complex transpeptidase PBPH, resulted in loss of cell viability (*SI Appendix*, Fig. S1). However, in the presence of 5 to 7.5 μM IPTG, growth was impaired without affecting viability (*SI Appendix*, Fig. S1). Using this sensitized condition, we performed a Tn-seq screen for insertions that resulted in loss of viability (synthetic lethality) or that improved growth (suppressors). We generated diverse transposon libraries in wild-type (WT) and the PBP2A depletion strain propagated with 100 μM IPTG. The libraries were then plated on LB agar plates supplemented with 6 μM IPTG, separately pooled, and Tn insertions mapped by next generation sequencing. Fig. 1*B* depicts all the genes for which the Tn insertions were significantly over or underrepresented in the strain with reduced levels of PBP2A compared to the WT. The screen identified a large and diverse set of genes previously implicated in cell envelope biogenesis, cell signaling, DNA replication and repair, RNA processing, metabolism, as well as genes of unknown function (Dataset S1 and *SI Appendix*, Fig. S2). To aid in viewing and evaluating these and other Tn-seq datasets, we developed a web-tool called TnSeeker (*SI Appendix*, Fig. S3 and *Materials and Methods*, rudnerlab.med.harvard.edu/tnseeker/). This tool allows users to upload a table of reads mapped to genomic position and displays the frequency of transposon insertions across the genome. In addition, it provides gene annotation via Genbank and Uniprot, allowing rapid and informative visual exploration of Tn-seq datasets.

In parallel, we performed eight one-by-all AF-M screens folding each Rod complex bait protein (RodA, PBP2A, MreC, MreD, RodZ, MreB, Mbl, MreBH) pairwise against the entire *B. subtilis* proteome. This in silico screen generated 33,437 individual predictions (Dataset S2). We ranked these predictions by their average predicted alignment error (pAE) across the predicted interface, a metric that agrees well with the predicted interface template modeling score (ipTM) but is not impacted by interface size. The predictions were separately ranked based on their average models score, a metric for how well the five models generated for each prediction agreed with one another (Fig. 1*C*) (34). Using an average models score above 4 and an average pAE below 5 Å, 10 of the 41 predictions were experimentally characterized interactions between members of the Rod complex and 4 predictions were between noncognate SEDS–bPBP pairs (Fig. 1*C* and *SI Appendix*, Fig. S4). We therefore used these cutoffs to define our highest confidence list of potential Rod complex interactors (*SI Appendix*, Table S1).

We cross-compared the 27 hits from the AF-M screen with our Tn-seq screen and found five genes that were hits in both (*SI Appendix*, Table S1). Of these, we discounted one (FabI) as AF-M predicted an interaction between this cytoplasmic protein and the extracytoplasmic region of RodZ. Another (YjbL) we did not analyze further as visual inspection of the Tn-insertion profile did not reveal strong differences between the WT and PBP2A deplete condition. Two of the final three interactors were of unknown function (YerH, YaaL), and one was a component of a manganese ABC transporter (MntA). In agreement with the Tn-seq, deletion mutations in *yerH* and *yaaL* modestly impaired growth in the PBP2A depletion strain and deletion of *mntA* modestly suppressed growth (*SI Appendix*, Fig. S5). We focused on YerH. Based on our characterization described below, we have renamed this factor ClcR for CamS lipoprotein cofactor for the Rod complex.

ClcR is a lipoprotein of unknown function. However, it has been suggested to function in cell division based on its genetic interaction with a component of the divisome and the actin homolog Mbl (35). Transposon insertions in *clcR* are underrepresented in the strain with reduced PBP2A levels (Fig. 1*D*), suggesting it plays a role in supporting Rod complex function when PBP2A is limiting. In addition, ClcR was strongly predicted to interact with the transpeptidase domain of PBP2A (Fig. 1*E*). Further analysis revealed that ClcR is predicted to form a highly confident tail-to-tail dimer and that this dimer is predicted to interact with PBP2A (*SI Appendix*, Fig. S6). AlphaFold3 also predicted a high-confidence PBP2A–$ClcR_2$ complex, a RodA–PBP2A–$ClcR_2$ complex, as well as the entire assembled Rod complex (RodA–PBP2A–$ClcR_2$–MreC–MreD–RodZ–$MreB_4$) (*SI Appendix*, Fig. S6). Importantly, the functionally redundant Rod complex transpeptidase PBPH, but not the divisome transpeptidase PBP2B, was also predicted to interact with ClcR (*SI Appendix*, Fig. S6). These data argue that ClcR may specifically function in the Rod complex.

ClcR Is Conserved in Diverse Gram-Positive Bacteria. ClcR is broadly conserved among gram-positive Bacillota (Fig. 2*A* and *SI Appendix*, Fig. S7). Furthermore, AlphaFold3 predicts high-confidence

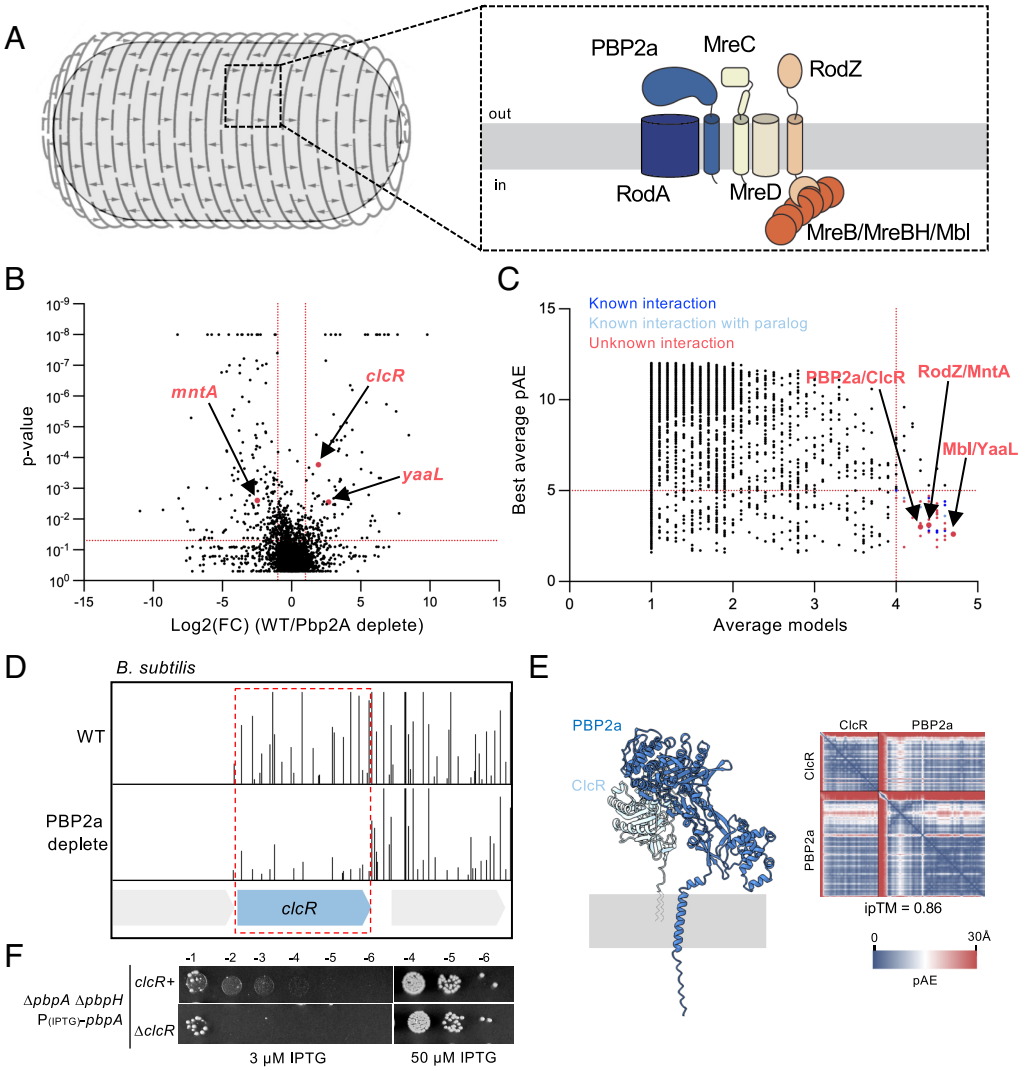

Fig. 1. Paired AF-M and Tn-seq screens identify ClcR as a potential Rod complex component. (*A*) Schematic of a peptidoglycan encased rod-shaped bacterium and essential members of the Rod complex in *B. subtilis*. (*B*) Scatter plot showing the fold change (FC) in transposon insertions between WT and cells with low levels of PBP2a. Red lines indicate a FC > 2 and a *P*-value < 0.05. All significant hits are listed in Dataset S1. The three hits that met our confidence metrics for the Tn-seq and AF-M screen are indicated. (*C*) Scatter plot showing the combined results of the eight one-vs.-proteome AF-M screens. Red lines indicate an average pAE value ≤ 5 Å and an average models score ≥ 4. The three hits that met our confidence metrics in both screens are indicated. Metrics from all predictions are available in Dataset S2. (*D*) Transposon-insertion profiles from the genomic region encoding *clcR* in *B. subtilis*. The height of the black lines indicates the number of reads mapped to that genomic position. (*E*) Alphafold2-predicted model and pAE plot of the ClcR–PBP2a interaction. The membrane is shown in gray. (*F*) Spot dilutions of the indicated *B. subtilis* strains on LB no salt agar supplemented with the indicated IPTG concentrations.

interactions between ClcR homologs and their cognate Rod complex bPBPs, including in *Listeria monocytogenes*, *S. aureus*, *B. anthracis, Lactobacillus crispatus, Aerococcus christensenii, and Erysipelothrix rhusiopathiae* (*SI Appendix*, Figs. S7 and S8). To investigate whether *clcR* genetically interacts with the Rod complex in other bacteria, we analyzed published Tn-seq datasets from *S. aureus* and *B. anthracis* (36, 37). The Rod complex is nonessential for growth in *S. aureus*, but its deletion results in hypersensitivity to the drug moenomycin, which targets the glycosyltransferase activity of aPBPs (38, 39). Analysis of a Tn library treated with subinhibitory concentrations of moenomycin identified Rod complex genes *rodA*, *pbp3*, encoding the Rod complex bPBP, and *mreCD* as critical for growth (*SI Appendix*, Fig. S9) (36). Strikingly, insertions in *clcR* (*camS*) were also significantly depleted in cells treated with moenomycin (Fig. 2*B*). We generated null mutations in *pbp3* and *clcR* and validated the Tn-seq. Both were sensitive to moenomycin, with Δ*clcR* showing an intermediate phenotype (Fig. 2*C*). Importantly, Δ*pbp3* was epistatic to Δ*clcR*, consistent with the idea that these genes function in the same pathway (Fig. 2*C*).

Unlike other Bacillota, *B. anthracis* and related species in the *Bacillus* A genus (*SI Appendix*, Fig. S10) encode two ClcR paralogs. One is syntenic with its homologs in *B. subtilis* and *S. aureus* (named *clcR1*), and the other is located at a distinct genomic position (named *clcR2*). Both are predicted to interact with the two bPBPs most closely related to PBP2A and PBPH from *B. subtilis* (*SI Appendix*, Fig. S8). Surprisingly, analysis of a WT *B. anthracis* Tn library (37) revealed virtually no Tn insertions in either gene, indicating that both paralogs are critical for the proper growth of *B. anthracis* (Fig. 2*D*). To characterize these genes, we used a non-pathogenic *B. anthracis* Sterne strain that lacked both virulence plasmids (see Methods). We constructed IPTG-regulated alleles of each and inserted them at a neutral chromosomal locus and then deleted the native *clcR* gene. Depletion of ClcR1 revealed a subtle growth defect resulting in smaller colony size, but no change in viability. Depletion of ClcR2 resulted in severely impaired growth and a 2-log defect in cell viability (Fig. 2*E*). Given

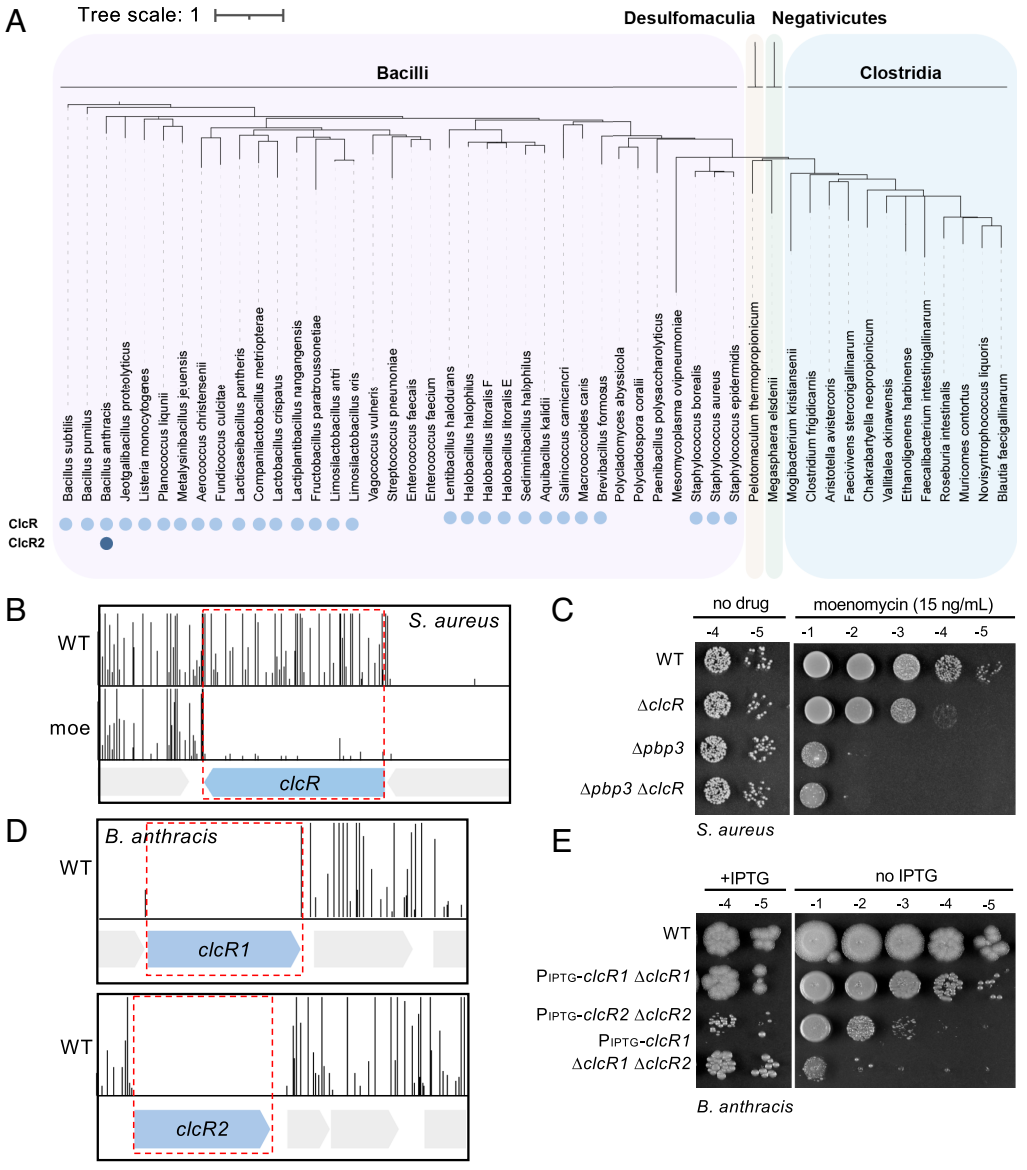

Fig. 2. ClcR is conserved in *S. aureus* and *B. anthracis*. (*A*) Phylogenetic tree of organisms from the Bacillota phylum with ClcR homologs indicated. Selected species represent the diversity reported in the Genome Taxonomy Database (GTDB). (*B*) Transposon-insertion profiles for the genomic region encoding *clcR* in *S. aureus* from a WT *S. aureus* library and one treated with 8 ng/mL moenomycin (moe) (36). The height of the black lines indicates the number of reads mapped to that genomic position. (*C*) Spot dilutions of the indicated *S. aureus* strains spotted on TSA with 15 ng/mL moenomycin or no drug. (*D*) Transposon insertion profiles for the genomic regions encoding *clcR1* and *clcR2* in a WT *B. anthracis* transposon library (37). (*E*) Spot dilutions of the indicated *B. anthracis* strains on BHI agar containing 0 or 500 μM IPTG.

that neither gene was strictly essential for growth under these conditions, we constructed a strain lacking both *clcR* genes harboring an IPTG-regulated *clcR1* allele. In the presence of 500 μM IPTG, Δ*clcR1* Δ*clcR2* PIPTG-*clcR1* cells were healthier than Δ*clcR2* cells, indicating that the increased levels of ClcR1 partially suppressed the absence of ClcR2. Furthermore, depletion of ClcR1 in the double mutant resulted in near total loss of viability (Fig. 2*E*). Taken together, these data indicate that the ClcR paralogs are functionally redundant and essential for the growth of *B. anthracis*.

ClcR Homologs Are Critical for Proper Cell Elongation. Deletion of *clcR* in the PBP2A depletion strain in *B. subtilis* resulted in only a modest loss of cell viability. To identify a stronger mutant phenotype to assay function, we treated WT and Δ*clcR* cells with a panel of cell envelope targeting antibiotics (*SI Appendix*, Fig. S11). We found that cells lacking ClcR were highly sensitive to several antibiotics, including the beta-lactam oxacillin (Fig. 3*A*), which targets the transpeptidase activity of the PBPs. As deletion of *pbpA* also results in increased sensitivity to oxacillin (Fig. 3*A*), we hypothesized that the sensitivity of the *clcR* mutant was due to impaired PBP2A activity. In agreement with this model, overexpression of PBP2A in cells lacking *clcR* partially suppressed the sensitivity to oxacillin (Fig. 3*B*). Importantly, this suppression was specific: overexpression of PBP2b, the cognate bPBP for the divisome, in the Δ*clcR* mutant did not change oxacillin resistance (Fig. 3*B*).

The Rod complex plays a central role in maintaining cell shape; its disruption leads to morphological defects. Accordingly, we investigated whether ClcR functions to maintain proper cell shape. To do so, we used our PBP2A depletion strain and expressed the transpeptidase at levels similar to those used in our Tn-seq screen (7.5 μM IPTG). Under these conditions, the cells looked indistinguishable from WT (Fig. 3*C*). However, deletion of *clcR* in this background resulted in shorter cells with increased width, as well as a cell-twisting phenotype (Fig. 3*C*). These phenotypes are consistent

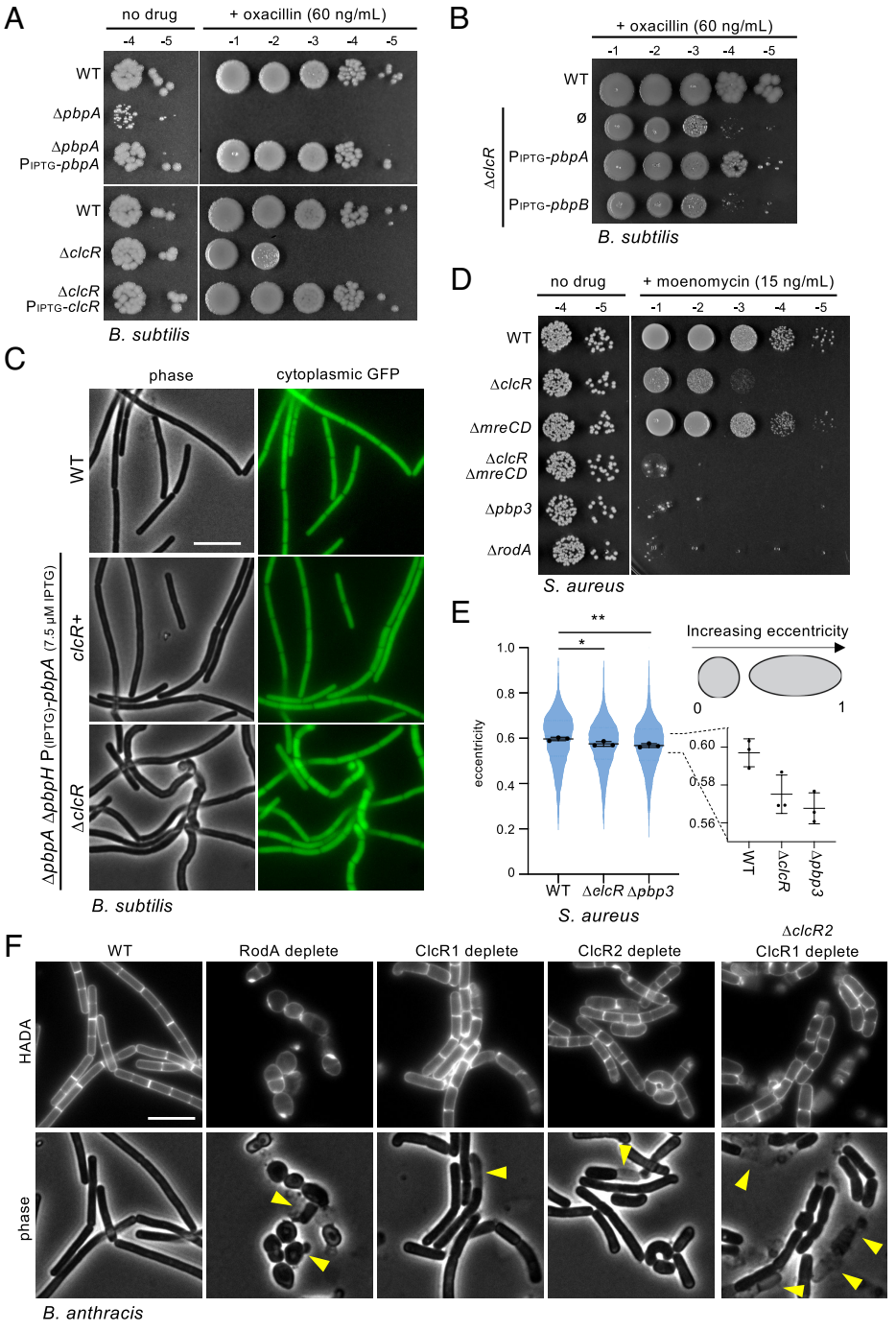

Fig. 3. ClcR is important for elongation in diverse gram-positive species. (*A* and *B*) Spot dilutions of the indicated strains on LB agar containing 500 μM IPTG and 60 ng/mL oxacillin or no drug. (*C*) Representative fluorescent and phase-contrast micrographs of WT *B. subtilis* and cells with low levels of PBP2a as the sole Rod complex bPBP in the presence or absence of *clcR*. (*D*) Spot dilutions of the indicated *S. aureus* strains on TSA containing 0 or 15 ng/mL moenomycin. (*E*) Violin plot showing the measured eccentricities of the indicated *S. aureus* strains. The blue plot represents all individual measurements across the three biological replicates, and each black point represents the average eccentricity of a given replicate. The center of error represents the average, and the error bars represent the SD among the replicates. The *Inset* shows the same results with an expanded y-axis. Shapes associated with changes in eccentricity are schematized above the plot. All measurements were made from *S. aureus* cells expressing a cytoplasmic GFP reporter and labeled with nile red membrane dye as seen in *SI Appendix*, Fig. S13. (*F*) Representative fluorescent and phase-contrast images of the indicated *B. anthracis* strains. Depletion strains were grown in the presence of IPTG for 2 h before backdilution into medium lacking IPTG and were imaged 1.5 h later. The cell wall was labeled by growth in medium containing 100 μM HADA for 15 min prior to imaging. Scale bars indicate 5 μm. Yellow carats indicate lysed cells.

with a reduction in Rod complex activity (40) and argue that ClcR functions in cell wall elongation. Although PBP2A is the dominant transpeptidase during exponential growth, *B. subtilis* encodes the functionally redundant PBPH, which is sufficient for Rod complex activity (3). Cells lacking both *pbpA* and *clcR* have a subtle growth defect compared to cells lacking *pbpA* alone, indicating that *clcR* is critical when PBPH is the sole Rod complex bPBP (*SI Appendix*, Fig. S12*A*). Using a Δ*pbpA* Δ*pbpH* strain harboring an IPTG-regulated allele of *pbpH*, we found that deletion of *clcR* resulted in a reduction in viability when PBPH was expressed at low levels (*SI Appendix*, Fig. S12*B*). Furthermore, these cells had severe morphological defects compared to the matched *clcR*$^{+}$ strain (*SI Appendix*, Fig. S12*C*). We conclude that ClcR is required for proper cell elongation in the presence of either Rod complex bPBP.

To investigate whether ClcR function is conserved, we generated mutations in the genes encoding Rod complex components in *S. aureus*. As previously shown, deletion of *rodA* or *pbp3* results in enhanced sensitivity to moenomycin (39), and loss of *clcR* confers an intermediate level of sensitivity (Fig. 3*D*). Surprisingly, we found that deletion of the regulators *mreC* and *mreD* conferred only a slight increase in moenomycin sensitivity, less than that of Δ*clcR* (Fig. 3*D*). Importantly, deletion of both *clcR* and *mreCD* were additive and resulted in moenomycin sensitivity equivalent to Δ*rodA* or Δ*pbp3*. These data suggest that ClcR's function is more critical for Rod complex activity than the conserved MreCD regulators in *S. aureus*. Our findings further suggest that ClcR and MreCD regulate RodA-PBP3 via distinct mechanisms. Deletion of Rod complex components in *S. aureus* has been shown to result

in a modest reduction in cell eccentricity (i.e., an increase in cell roundness) due to the loss of cell wall elongation proximal to the cell septum (39, 41). We quantified this parameter in our Δ*pbp3* and Δ*clcR* mutants and observed a subtle decrease in eccentricity in both mutants compared to WT as reported previously (Fig. 3*E*). Collectively, these data argue that, like in *B. subtilis*, ClcR is required for the proper function of the Rod complex in *S. aureus*.

Finally, we investigated whether the *B. anthracis* mutants lacking the ClcR paralogs have morphological defects consistent with impaired Rod complex function. As is the case in *B. subtilis,* (2, 42) depletion of the *B. anthracis* RodA PG polymerase resulted in cell shortening and rounding prior to lysis (Fig. 3*F*). Depletion of either ClcR paralog alone resulted in cells with reduced length and increased width, along with cell rounding (Fig. 3*F*) with ClcR2 having a greater impact on cell shape. These results, along with the cell viability data (Fig. 2*E*) argue that ClcR2 is more critical for Rod complex function than ClcR1. Importantly, depletion of ClcR1 in the absence of *clcR2* resulted in cell rounding followed by lysis, similar to that of the RodA depletion. These dramatic phenotypes are consistent with an essential role for the ClcR paralogs in Rod complex stability, assembly, or cell wall synthesis in *B. anthracis*.

ClcR Interacts with Elongation-Specific bPBPs. *B. subtilis* ClcR was previously identified as one of many factors that could be formaldehyde-crosslinked to the MreB paralogs in vivo (43). To investigate a direct interaction between ClcR and PBP2A, as AF-M predicts, we used the Bacterial Adenylate Cyclase Two Hybrid (BACTH) interaction assay (44). We generated fusions of the soluble extracytoplasmic domains of ClcR and PBP2A to complementary fragments (T18 and T25) of *Bordetella pertussis* adenylate cyclase and analyzed their interaction in *E. coli* on LB+X-gal plates. We identified positive interactions between PBP2A and ClcR and PBPH and ClcR but not control fusions (Fig. 4*A*). In addition, ClcR interacted with itself, supporting the model that it functions as a dimer. To directly test the Alphafold-predicted model, we generated a point mutation (R76E) at the predicted interaction interface between ClcR and PBP2A (Fig. 4*B*). This mutant lost the ability to interact with PBP2A but not with itself (Fig. 4*C*). We conclude that PBP2A and ClcR interact.

To investigate the biological relevance of the interaction between PBP2A and ClcR, we expressed the interface-breaking mutant *clcR*^{R76E} in *B. subtilis* and found that it failed to complement the Δ*clcR* sensitivity to oxacillin (Fig. 4 *D* and *E*). An amino acid substitution of the analogous residue (serine-76) to glutamate (S76E) in *S. aureus* ClcR similarly disrupted ClcR function as assayed by moenomycin sensitivity (Fig. 4 *F* and *G*). These results indicate that the interaction between ClcR and the Rod complex bPBP is critical for ClcR function.

A ClcR Variant Hyperactivates PBP2A. The experiments described above led us to hypothesize that ClcR impacts PBP2A stability or activity. To investigate the former possibility, we analyzed the levels of all PBPs using a fluorescent analog of penicillin, Bocillin-FL. Visualization of the Bocillin-FL-labeled PBPs by SDS-PAGE revealed no change in levels of the Rod complex bPBPs (or any PBPs) upon deletion of *clcR* in *B. subtilis* or *S. aureus* (Fig. 5*A*). Furthermore, all *B. anthracis* PBPs remained stable in the absence of *clcR1* or *clcR2* (Fig. 5*A*). We conclude that ClcR does not impact the stability of its cognate bPBP and therefore likely regulates its activity.

If ClcR positively regulates PBP2A activity, we reasoned that we should be able to identify *clcR* mutations that stimulate PBP2A function. Such mutations are predicted to increase oxacillin resistance. Accordingly, we generated a PCR-mutagenized library of *clcR* and selected for oxacillin resistant mutants (Fig. 5*B*). We isolated 12 mutants, 10 of which validated upon backcrossing

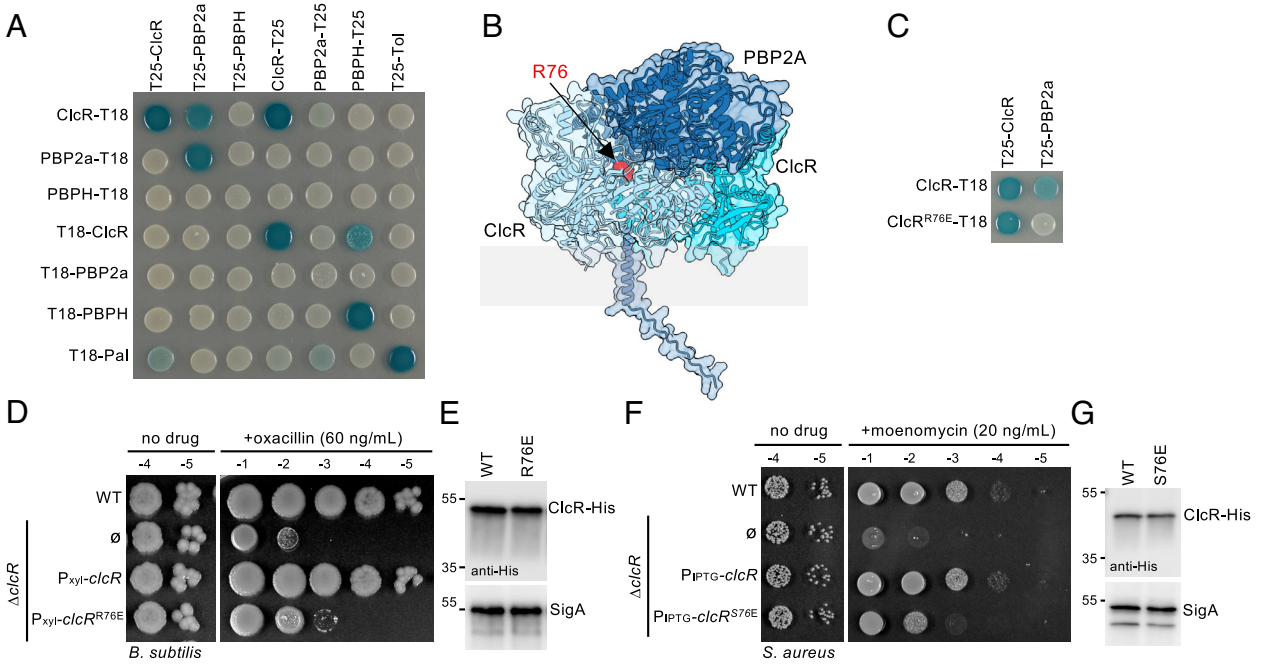

Fig. 4. ClcR interacts with Rod complex bPBPs. (*A*) *E. coli* cells (BTH101) containing plasmids expressing the indicated T25 and T18 fusions were grown overnight in LB supplemented with 30 μg/mL kanamycin, 100 μg/mL ampicillin, and 500 μM IPTG prior to spotting onto LB agar containing the same supplements and 100 μg/mL X-gal. (*B*) Alphafold3 model of the ClcR$_2$–PBP2a complex with the interface residue R76 highlighted in red. (*C*) BTH101 *E. coli* cells expressing the indicated variants were assayed as described in (*A*). (*D*) Spot dilutions of the indicated *B. subtilis* strains on LB agar containing 20 mM xylose and 60 ng/mL oxacillin or no drug. (*E*) Representative immunoblot of *B. subtilis* cells expressing functional His-tagged ClcR (*SI Appendix*, Fig. S14) variants expressed from an IPTG-regulated promoter with 500 μM IPTG. SigA controls for loading. (*F*) Spot dilutions of the indicated *S. aureus* strains spotted on TSA containing 500 μM IPTG and 20 ng/mL moenomycin or no drug. (*G*) Representative immunoblot of *S. aureus* cells expressing functional His-tagged ClcR (*SI Appendix*, Fig. S14) or ClcR(S76E)-His from an IPTG-regulated promoter with 500 μM IPTG. SigA controls for loading. Molecular weight markers in kDa are indicated.

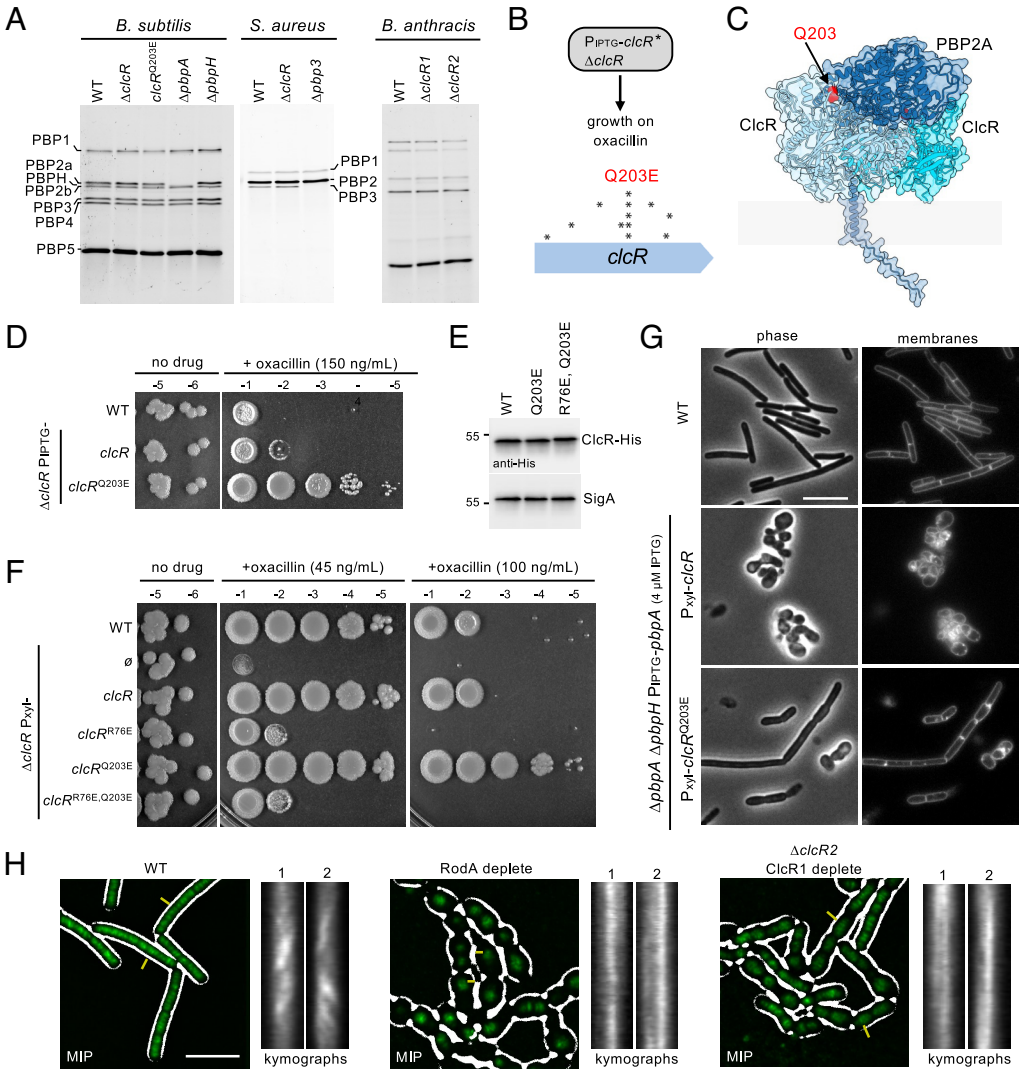

Fig. 5. ClcR positively regulates Rod complex activity. (*A*) Representative gels of Bocillin-FL-labeled PBPs in the indicated strains of *B. subtilis*, *S. aureus*, and *B. anthracis*. *B. anthracis* PBPs are unlabeled because the proteins have not been named. The *B. subtilis* ClcR^{Q203E} mutant is expressed from an IPTG-regulated promoter with 500 μM IPTG. (*B*) Schematic for the screen to identify *clcR* alleles with increased oxacillin resistance. A PCR-mutagenized *clcR* library was transformed into *B. subtilis* and then selected for growth on 200 ng/mL oxacillin. Five independent suppressors contained the Q203E mutation. Asterisks indicate the positions of mutations in each suppressor. (*C*) Alphafold3 model of the $ClcR_2$–PBP2a complex with the identified Q203 residue highlighted in red. (*D*) Spot titers of the indicated strains on LB containing 500 μM IPTG and 150 ng/mL oxacillin or no drug. (*E*) Representative immunoblot of *B. subtilis* cells expressing the indicated His-tagged variants of ClcR from an IPTG-regulated promoter with 500 μM IPTG. SigA controls for loading. Molecular weight markers are indicated in kDa. (*F*) Spot titers of *B. subtilis* cells expressing the indicated *clcR* mutants from a xylose-regulated promoter. LB agar plates contain 20 mM xylose and 0, 45, or 100 ng/mL oxacillin. (*G*) Phase and fluorescent micrographs of *B. subtilis* WT cells or those expressing PBP2a with 4 μM IPTG in the absence of *pbpH*. Where indicated, cells also express ClcR or ClcR^{Q203E} from a xylose-regulated promoter with 20 mM xylose. Membranes are labeled with 50 μM TMA-DPH. (*H*) Particle tracking of Mbl-mNg in the indicated *B. anthracis* strains. (*Left*) MIP of movies of Mbl-mNg taken every 1 s for 2 min (Movies S1–S3). Cells are outlined using a threshold generated from a brightfield image taken of the same cells. (*Right*) Kymographs showing particle movement over time for two representative particles. Yellow lines on the MIP indicate positions of the kymographs which were generated at the horizontal cross-section of the cell using one pixel width. All scale bars indicate 5 μm.

into the parental strain. Sequencing revealed that all validated mutants had a point mutation in *clcR* resulting in a substitution of asparagine 203 to glutamate (*clcR*^{Q203E}) (Fig. 5*B*). This residue lies proximal to the predicted interaction interface of ClcR and PBP2A (Fig. 5*C*). ClcR^{203E} increased cell viability upon treatment with 150 ng/mL oxacillin by ~1,000-fold (Fig. 5*D*) and did so without changing PBP2A or ClcR levels (Fig. 5 *A* and *E*). Importantly, the interaction-disrupting mutation *clcR*^{R76E} was epistatic to the oxacillin-resistant *clcR*^{Q203E} allele (Fig. 5*F*), indicating that the hyperactivity of *clcR*^{Q203E} requires interaction with PBP2A. These findings are consistent with the idea that ClcR positively regulates PBP2A.

To test whether ClcR^{203E} could restore shape to cells expressing low levels of PBP2A, we expressed *clcR* or *clcR*^{Q203E} from a xylose-regulated promoter in strains harboring an IPTG-regulated *pbpA* allele. At very low concentrations of IPTG (4 μM), the cells expressing WT ClcR had gross morphological defects that included increased cell width, decreased cell length, and cell twisting. By contrast, cells expressing ClcR^{Q203E} were more rod shaped, similar to WT (Fig. 5*G*). These results support the model that ClcR^{203E} increases PBP2A activity and thus Rod complex function.

ClcR Is Required for the Dynamic Movement of the Rod Complex in *B. anthracis*. Our data argue that ClcR positively regulates PBP2A activity to support Rod complex-mediated PG synthesis. However, ClcR is only required in *B. subtilis* and *S. aureus* under conditions in which PG synthesis is partially impaired. By

contrast, the ClcR paralogs are critical for growth in *B. anthracis*. We therefore investigated whether the *B. anthracis* paralogs are required for Rod complex function. To do so, we monitored the dynamic behavior of the cell wall elongation machinery, using single particle tracking of the MreB paralog Mbl. We generated a native Mbl-mNeongreen (Mbl-mNg) fusion in *B. anthracis* and tracked the fluorescent Mbl-mNg foci by TIRF microscopy. As anticipated, Mbl-mNg particles moved circumferentially around the long axis of the cell (Fig. 5*H* and Movie S1) in a manner similar to the MreB paralogs in *B. subtilis* (11, 12). Next, we imaged Mbl-mNg in cells depleted of RodA. Most particles were immobile by 2 h of depletion (Fig. 5*H* and Movie S2), as observed previously in *B. subtilis* (11). Finally, we imaged Mbl-nNg, upon depletion of ClcR1 in the absence of ClcR2. Similar to the RodA depletion, most Mbl-nNg fluorescent foci were immobile after 2 h of depletion (Fig. 5*H* and Movie S3). These data indicate that the *B. anthracis* ClcR paralogs are required for Rod complex-mediated PG synthesis and suggest they are a core component of the cell elongation machinery in this bacterium.

Discussion

Altogether, our characterization of ClcR homologs in *B. subtilis*, *S. aureus*, and *B. anthracis* has defined a broadly conserved member of the Rod complex. Our findings support the model that ClcR interacts with and positively regulates the bPBP transpeptidase of the Rod complex, stimulating the cell wall elongation machinery. Our study also provides a method to identify functionally relevant protein–protein interactions by pairing high-throughput genetics with in silico protein–protein interaction screening.

Large scale AF-M screens for protein–protein interactions have revolutionized molecular biology research. However, because false-positive interactions are common, methods have been developed to help prioritize predicted interactions that are likely to be biologically relevant (45, 46). In eukaryotes, successful methods to classify predicted interactions include the use of data from CRISPR screens, coexpression studies, subcellular localization, and high throughout interaction experiments (45). Our AF-M screens in *B. subtilis* identified a large number of confident protein–protein interactions, likely more than are biologically relevant (Dataset S2). Similarly, our Tn-seq screen identified >350 significant hits with a fold-change ≥ 2 or ≤ 0.5 (Dataset S1). Either screen performed alone would not have easily identified important Rod complex regulators. Pairing the two efficiently prioritized hits for validation.

Our study provides a nice example of how homologous proteins in different organisms have similar function but make distinct contributions to a biological process. ClcR contributes to Rod complex activity in *B. subtilis* but is not critical for cell wall synthesis. In *S. aureus*, the Rod complex itself is not essential, but ClcR is more important for RodA-PBP3 function than MreC and MreD. Finally, the activity of the ClcR paralogs in *B. anthracis* are essential for growth and maintaining rod shape. These findings underscore the importance of complementing research in model organisms with mechanistic studies in human pathogens and other nonmodel bacteria.

It is noteworthy that ClcR homologs have been studied since the 1980s. In *S. aureus*, a peptide is produced from the ClcR lipidation signal peptide (47). After the peptide, called cAM373, is processed and secreted it acts as a pheromone to induce clumping of *E. faecalis* cells that carry the sex pheromone plasmid pAM373. Clumping promotes gene transfer between the two species. Thus, *clcR* in *S. aureus* was originally named *camS* (cAM373 in S. *aureus*). It was long hypothesized that the CamS (ClcR) protein product had an unrelated function, as the peptide is only encoded in certain *S. aureus* species and is not found in the lipidation sequence of any of the other diverse species that have a *clcR* homolog (48). To ensure that the phenotypes reported here were due to the lipoprotein product and not the peptide, we generated in-frame deletions that retained the lipidation sequence in both *S. aureus* and *B. subtilis*. The mutants remained sensitive to moenomycin and oxacillin, respectively (*SI Appendix*, Fig. S15), indicating that the ClcR lipoprotein is required to regulate Rod complex bPBPs.

The mechanism by which ClcR activates its cognate bPBP is currently unknown. The AlphaFold model predicts that ClcR largely interacts with PBP2A's transpeptidase region, which is distinct from the predicted interaction region with MreC in the pedestal domain. However, ClcR is not predicted to occlude PBP2A's active site. Recent single molecule studies have revealed the conformational dynamics that underpin the regulation of SEDS–bPBP pairs (10). The membrane complex exists in two states. In the inactive "down" state the bPBP resides close to the membrane and occludes the glycosyltransferase active site of the SEDS polymerase. In the active "up" state, the bPBP's active site is positioned adjacent to the peptidoglycan meshwork, the glycosyltransferase active site is accessible, and the polymerized strand can be passed from the glycosyltransferase to the transpeptidase domain to be crosslinked (8, 10). It has been proposed that the interaction of MreC with PBP2A's pedestal domain promotes the transition of the complex into the active state (9). By analogy, we hypothesize that ClcR, bound underneath the transpeptidase domain, can similarly promote the transition of PBP2A into the "up" active conformation. All AlphaFold predictions for ClcR–bPBP interactions predict the bPBP in the "up" state. In the context of this model, we speculate that the ClcR^{Q203E} variant stabilizes PBP2A in its up state, thereby constitutively activating PG synthesis.

In addition to ClcR, we identified two genes, *yaaL* and *mntA*, which met the requirements of putative Rod complex regulators in the AF-M and Tn-seq screens. YaaL is a small protein with two predicted alpha helices that interacts with Mbl near its oligomerization interface. Future work will determine whether this small protein modulates Mbl assembly or dynamics. MntA is a lipoprotein component of a manganese ABC transporter which was predicted to interact with the extracellular domain of RodZ. A connection between Rod complex synthesis and manganese transport remains to be investigated, but notably each component of the manganese transporter was enriched in insertions in the PBP2A depletion condition (*SI Appendix*, Fig. S5*B*).

We note that the previously reported *B. subtilis* Rod complex regulators TseB and RagB were not identified by the paired AlphaFold and Tn-seq screens with the cutoffs used to identify high priority hits. However, both TseB and RagB were predicted with lower confidence scores to interact with PBP2A and RodA, respectively (Dataset S2). In addition, *tseB* was a hit in the Tn-seq screen with an 8.7-fold decrease in insertions in the PBP2A deplete condition (Dataset S1). These data indicate that additional unknown regulators of the Rod complex may exist in our dataset but fell below the confidence metric cutoffs used in this study. The challenge for the future is to identify the full set of factors that modulate Rod complex activity across bacteria and determine how they function to control the cell wall elongation machinery in diverse organisms with distinct morphologies.

Materials and Methods

All *B. subtilis* strains were derived from the prototrophic strain PY79 (49). All *S. aureus* strains were derived from the NCTC8325 derivative HG003 (50). All *B. anthracis* strains were derived from the plasmid-free non-pathogenic, avirulent Sterne derivative *B. anthracis* 9131 called BaR1 (37). General methods as well as tables of strains, plasmids, and oligonucleotide primers and a description of strain and plasmid construction can be found online as *SI Appendix*, Tables S1–S4 and Text S1.

TnSeeker. TnSeeker is available at rudnerlab.med.harvard.edu/tnseeker/. Additional information about the application can be found in *SI Appendix*, Text S1.

Statistics and Reproducibility. All experiments were carried out in biological triplicate. For fluorescence microscopy, all experiments were carried out in biological triplicate, and at least 10 fields of view imaged and analyzed when quantified.

Tn-seq. Tn-seq was performed as described previously (51, 52). In brief, pWX642 containing a Mariner transposon and transposase was transformed into *B. subtilis* and selected on LB+erythromycin+lincomycin. Several colonies were pooled and rolled for 20 h in LB+spectinomycin at 22 °C before freezing in 14% glycerol. Cells were thawed and plated onto LB+spectinomycin at 42 °C to select for cells that have integrated the transposon and lost the plasmid. Approximately 750,000 individual colonies were pooled and their genomic DNA isolated (Blood and Tissue kit, Qiagen). Each sample was digested with MmeI (NEB), barcode-containing adapters ligated, Transposon–gDNA junctions amplified using universal primers binding the transposon and adapter sequences, and the product gel purified before loading onto an Illumina NextSeq2000. The reads were demultiplexed, normalized between libraries, trimmed, and mapped to the *B. subtilis* PY79 genome. Total reads across genes were pooled to determine the ratio of reads between WT and PBP2A deplete libraries, and statistical significance was determined using a Mann–Whitney *U* test corrected for multiple hypothesis testing.

AF-M Screening. The one-by-all Alphafold screens were performed pairwise using the 8 bait proteins (P39604, P54488, Q01466, Q01467, O31771, Q01465, P39751, P39763) against the Uniprot *B. subtilis* 168 proteome (UP000001570). The screen was performed using colabfold version 1.5.5 (53–55). Each prediction was run with five models, using three recycles, no dropout, no templates. These runs were performed using a local installation of Colabfold running on NVIDIA A6000 GPUs managed by the HMS O2 computing cluster. MSAs were generated using MMseqs2 API server (56). All predictions used paired and unpaired MSAs, and structures were unrelaxed. To analyze the results of the pairwise screen, we utilized a published analysis pipeline (34). Predictions were considered in contact if they had an average models score ≥ 1 and were considered high-confidence hits if they had an average models score ≥ 4 and an average pAE ≤ 5 Å. The results of all predictions are available in Dataset S2 with ipTM values listed for all predictions and average models and best average pAE values listed for those considered in contact.

Spot Titers. Cells were cultured to late-log phase in permissive conditions, washed 3× in LB, TSB, or BHI (rich medium), normalized to OD600 = 1.5, and diluted 10-fold in rich medium to 10^{-6}. 5.5 μL of each dilution were spotted onto LB, TSA, BHI agar supplemented with the indicated IPTG, xylose, and drug concentrations. Plates were incubated at 37 °C for 12 to 16 h before imaging. Images were adjusted to grayscale using photoshop.

Growth Curves. Cells were subcultured in 3 mL LB before backdilution into LB at OD600 = 0.005. 200 μL cells were added to individual wells of a clear polystyrene 96-well plate (Genesee) and plates were incubated shaking at 432 rpm at 37 °C in an Infinite M Plex microplate reader (Tecan). OD600 was monitored every 5 min for 18 h. Measurements were averaged at each timepoint across technical triplicates and plotted using excel. When cells contained antibiotics, it was typically at 0.5× MIC, as determined by a standard MIC assay. Otherwise, antibiotic concentrations were varied until there was clearly an impact on growth for WT cells.

Fluorescence Microscopy. Fluorescence microscopy was performed on a Nikon Ti2-E inverted microscope equipped with Plan Apo 100×/1.45 phase contrast oil objective and a Hamamatsu ORCA-Flash4.0 V3 Digital CMOS camera. Light was delivered with the Lumencor Spectra III Light Engine containing the following filters: 390/22, 440/20, 475/28, 510/25, 555/28, 575/25, 637/12, 748/12. Images were acquired using the Nikon Elements 5.2 acquisition software. Cells were cultured to mid-log phase (OD_{600} ~ 0.2–0.4), 1 mL of culture was collected (4,000 g/5 min) and concentrated into 50 μL media, and 5.5 μL of concentrated culture were immobilized using 2% agarose pads containing LB, TSB, BHI, CH, or PBS medium. Envelope integrity and peptidoglycan synthesis were monitored using 5 μM propidium iodide (PI) (Sigma) and 100 μM of the fluorescent D-amino acid HADA, respectively. For HADA labeling, cells were labeled in media containing 100 μM HADA for 15 min prior to washing and immobilizing on agarose pads. Membranes were detected either using the probe Nile Red at 1 μg/mL or the probe TMA-DPH at 50 μM (Fisher Scientific). Cytoplasm was labeled with constitutively expressed GFP when indicated. Images were cropped and adjusted using Fiji. All images shown side by side were acquired, analyzed, and adjusted, identically for comparison. Images are shown at a magnification of 100×.

Eccentricity Measurements. *S. aureus* containing a cytoplasmic GFP reporter and with their membranes labeled using Nile Red were imaged as described in the fluorescence microscopy section. These cells were segmented using the Cellpose cyto3 algorithm in mAIcrobe (57) based on the cytoplasmic GFP marker, and their morphology measured using the precomputed *S. aureus* membrane epifluorescence model. The mean eccentricity was calculated from n > 1,500 cells in each of three independent biological replicates and statistical significance was calculated using a student's *t* test across these means. The equation for calculation of eccentricity is ecc = sqrt(1 - (b^2/a^2)) where a is the semimajor axis and b is the semiminor axis.

Immunoblot Analysis. Immunoblot analysis was performed as described previously (58). Briefly, 1 mL of exponentially growing culture (OD_{600} ~ 0.5) was collected and resuspended in lysis buffer [20 mM Tris pH 7.0, 10 mM $MgCl_2$ and 1 mM EDTA, 1 mg/mL lysozyme (*B. subtilis*) or 20 μg/mL lysostaphin (*S. aureus*), 10 μg/mL DNase I, 100 μg/mL RNase A, 1 mM PMSF] to a final OD_{600} of 10 for equivalent loading. The cells were incubated at 37 °C for 15 min followed by addition of an equal volume of Laemelli sample buffer (0.25 M Tris pH 6.8, 4% SDS, 20% glycerol, 10 mM EDTA) containing 10% β-mercaptoethanol. Samples were heated for 15 min at 65 °C prior to loading. Proteins were resolved by SDS-PAGE on 12.5% polyacrylamide gels, electroblotted onto Immobilon-P membranes (Millipore) and blocked in 5% nonfat milk in phosphate-buffered saline (PBS) with 0.5% Tween-20. The blocked membranes were probed with anti-SigA (1:10,000) (59), anti-His (1:4,000) (GenScript), anti-ALFA (1:1,000) (Rabbit Fc conjugate, Nanotag) antibodies diluted into 3% BSA in PBS with 0.05% Tween-20. Primary antibodies were detected using horseradish peroxidase-conjugated goat anti-rabbit or anti-mouse IgG (BioRad) and the Super Signal chemiluminescence reagent as described by the manufacturer (Pierce). Signal was detected using a Bio-Techne FluorChem R System. Images were cropped and contrast adjusted using Fiji.

Bacterial Two-Hybrid. The Bacterial Adenylate Cyclase-based Two Hybrid (BACTH) system was used for two-hybrid analysis (44). Plasmids containing protein fusions to the *Bordetella pertussis* adenylate cyclase T25 and T18 fragments were cotransformed into BTH101 [F-, *cya-99, araD139, galE15, galK16, rpsL1 (Str r), hsdR2, mcrA1, mcrB1*]. Transformants were cultured in LB containing 100 μg/mL ampicillin, 25 μg/mL kanamycin, and 500 μM IPTG overnight at 30 °C. 5.5 μL of culture was spotted onto LB agar plates containing 100 μg/mL ampicillin, 25 μg/mL kanamycin, 500 μM IPTG, and 100 μg/mL and 5-bromo-4-chloro-3-indolyl-β-D-galactopyrannoside (X-Gal). Plates were imaged after 18-h incubation at 30 °C.

Bioinformatics Analysis. A tree consisting of 50 representative members of the Bacillota was subsampled from release 226 of GTDB taxonomy (60). The genomes of these organisms were downloaded from NCBI, and their protein coding regions identified using prodigal gene annotation (61). These proteins were used as the target for mmseq2 (56) searches with queries for BsClcR, BaClcR1, and BaClcR2. Relaxed cutoffs were used for homolog identification (c = 0.6, min-seq-id = 0.2, e-value= 1×10^{-3}), and results were manually inspected to ensure no false positives. Genomes encoding an ortholog meeting these requirements were annotated on the phylogenetic tree. Annotation of ClcR1 vs. ClcR2 was done using the reciprocal best hit to the *B. anthracis* proteins. Tree visualization and manipulation was done using iTOL (62).

Mutagenesis Screen to Identify *clcR* Alleles. The *clcR* gene was mutagenized using Mutazyme (Agilent) with the goal of obtaining 2 mutations/kb. The subsequent reaction was gel purified and then PCR amplified using Q5 polymerase (NEB). This product was assembled into a digested plasmid containing an IPTG inducible allele and homology arms for integration into the neutral *yhdG* locus using Hifi assembly (NEB). The assembled plasmids were transformed via electroporation into DH10b competent cells (NEB) and plated onto selective medium. ~1,000,000 colonies were pooled and their plasmid DNA isolated. The resulting plasmid library was linearized by digestion with ScaI and transformed via 1-step competence into *B. subtilis* cells lacking *clcR* to isolate ~50,000 individual colonies. Cells were pooled and frozen in 14% glycerol. For selection, cells were thawed and plated onto 100, 150, or 200 ng/mL oxacillin to obtain alleles with increased oxacillin resistance. Individual colonies were screened for IPTG dependence of oxacillin resistance before amplifying the *yhdG* locus and sequencing the *clcR* gene.

Bocillin-FL Assays. Cells were cultured to an OD600 of 0.5 and 10 mL of cells were pelleted and washed 1× with PBS before resuspension in 1 mL PBS + 15 μM Bocillin-FL (Invitrogen). Cells were incubated at 25 °C for 15 min and washed 3× with PBS. Cells were resuspended in PBS + 1 mg/mL lysozyme (*B. subtilis*) or 200 μg/mL lysostaphin (*S. aureus*) or 2 mg/mL lysozyme + 1 U Mutanolysin + 200 μg/mL lysostaphin (*B. anthracis*) and incubated at 37 °C for 30 min. Cells were further lysed by Bioruptor (Diagenode). Membranes were pelleted by ultracentrifugation at 100,000 g for 45 min at 4 °C. The membrane fraction was resuspended in 50 μL 1× Laemmli sample buffer and the total protein content was determined using the Ni-protein assay (G Biosciences). 20 μg total protein was incubated at 65 °C for 15 min prior to loading onto a 10% SDS-PAGE gel. Bocillin-labeled proteins were visualized using a Typhoon 9500 fluorescence imager (GE Healthcare) with excitation at 488 nm and emission at 530 nm. After imaging, the gel was stained for total protein content using Instant Blue (Abcam).

Mbl-mNeonGreen TIRF Imaging. Cells were cultured to mid-log in BHI before pelleting 1 mL, resuspending in 20 μL BHI and spotting under a 2% BHI agarose pad on 50 mm No. 1.5 cover glass dish (Matek). Cells were imaged on a Nikon Ti2E fully automated inverted microscope equipped with an iLAS Gataca System TIRF hardware add-on capable of Ring-TIRF illumination and a Tokai Hit Warming Box with a stage top humid chamber. TIRF imaging was performed at 37 °C. Images were acquired using the Nikon Elements acquisition software AR. Fluorescent signal from mNeonGreen was collected by illuminating the sample with a 488 nm laser line (Nikon LUN-F combiner) and using a TIRF 405/488/561/638 nm Quad Dichroic Mirror and a BP 525/50 nm emission filter. Timelapses were acquired with 200 ms exposure time every 1 s for 2 min at a TIRF angle of 60 nm. Images were processed using Fiji (63): Stage drift was corrected using StackReg (64), the background was subtracted using a rolling ball radius of 20 pixels, and maximum intensity projection (MIP) images from all 121 frames as well as kymographs from 1-pixel widths generated using MicrobeJ (65). A singular brightfield image taken prior to the time course was used to segment cells. For depletion experiments, cells were subcultured for 3 h in the presence of 500 μM IPTG, washed, and backdiluted into 25 mL BHI at OD600 = 0.025. Cells were imaged every hour after backdilution.

Data, Materials, and Software Availability. All confidence metrics resulting from the AF-M screens are included in *SI Appendix*. Raw data for all graphs have been uploaded as source data. Uncropped immunoblots are included in *SI Appendix*. Primers and strains used can be found in *SI Appendix*, Tables S1–S4. Raw transposon sequencing fastq files have been deposited in the Sequence Read Archive with accession PRJNA1435919 (66). All other data are included in the manuscript and/or supporting information.

ACKNOWLEDGMENTS. We thank all members of the Bernhardt-Rudner supergroup, especially Shailab Shrestha, for helpful advice, discussions, and encouragement. We thank Ethan Garner for the *B. subtilis mreB-mNeonGreen* fusion strain and Andrew Varble and Luciano Marrafini for the *S. aureus* recombineering plasmid pPM260. Portions of this research were conducted on the O2 High Performance Computing Cluster, which is supported by the Research Computing Group at Harvard Medical School. Microscopy was performed with help from the Microscopy Resources on the North Quad (MicRoN) core at Harvard Medical School. Support for this work comes from the National Institute of Health Grants R35GM145299, U19 AI158028 (D.Z.R.). A.P.B. was funded in part by NSF (DGE1745303) and NIH (F31AI181098).

1. P. D. A. Rohs, T. G. Bernhardt, Growth and division of the peptidoglycan matrix. *Annu. Rev. Microbiol.* **75**, 15.1–15.22 (2021).
2. A. J. Meeske *et al.*, SEDS proteins are a widespread family of bacterial cell wall polymerases. *Nature* **537**, 634–638 (2016).
3. Y. Wei, T. Havasy, D. C. McPherson, D. L. Popham, Rod shape determination by the Bacillus subtilis Class B penicillin-binding proteins encoded by pbpA and pbpH. *J. Bacteriol.* **185**, 4717–4726 (2003).
4. M. Leaver, J. Errington, Roles for MreC and MreD proteins in helical growth of the cylindrical cell wall in Bacillus subtilis. *Mol. Microbiol.* **57**, 1196–1209 (2005).
5. P. D. A. Rohs *et al.*, A central role for PBP2 in the activation of peptidoglycan polymerization by the bacterial cell elongation machinery. *PLoS Genet.* **14**, e1007726 (2018).
6. P. D. A. Rohs *et al.*, Identification of potential regulatory domains within the MreC and MreD components of the cell elongation machinery. *J. Bacteriol.* **203**, e00493-20 (2021).
7. M. S. A. Gilman *et al.*, Conformational regulation of two essential activators of bacterial cell elongation. *Proc. Natl. Acad. Sci. U.S.A.* **122**, e2514198122 (2025).
8. M. Sjodt *et al.*, Structural coordination of polymerization and crosslinking by a SEDS–bPBP peptidoglycan synthase complex. *Nat. Microbiol.* **5**, 813–820 (2020).
9. C. Contreras-Martel *et al.*, Molecular architecture of the PBP2–MreC core bacterial cell wall synthesis complex. *Nat. Commun.* **8**, 776 (2017).
10. I. Shlosman *et al.*, Allosteric activation of cell wall synthesis during bacterial growth. *Nat. Commun.* **14**, 3439 (2023).
11. E. C. Garner *et al.*, Coupled, circumferential motions of the cell wall synthesis machinery and MreB filaments in *B. subtilis*. *Science* **333**, 222–225 (2011).
12. J. Domínguez-Escobar *et al.*, Processive movement of MreB-associated cell wall biosynthetic complexes in bacteria. *Science* **333**, 225–228 (2011).
13. Y. Kawai, K. Asai, J. Errington, Partial functional redundancy of MreB isoforms, MreB, Mbl and MreBH, in cell morphogenesis of Bacillus subtilis. *Mol. Microbiol.* **73**, 719–731 (2009).
14. S. A. Alyahya *et al.*, RodZ, a component of the bacterial core morphogenic apparatus. *Proc. Natl. Acad. Sci. U.S.A.* **106**, 1239–1244 (2009).
15. K. Muchová, Z. Chromiková, I. Barák, Control of Bacillus subtilis cell shape by RodZ. *Environ. Microbiol.* **15**, 3259–3271 (2013).
16. R. Zhan *et al.*, RodZ acts through MreBCD to activate the elongasome in *Escherichia coli*. bioRxiv [Prepirnt] (2026). https://doi.org/10.64898/2026.01.05.697639 (Accessed 15 March 2026).
17. Y. Sun, S. Hürlimann, E. Garner, Growth rate is modulated by monitoring cell wall precursors in Bacillus subtilis. *Nat. Microbiol.* **8**, 469–480 (2023).
18. F. Pompeo *et al.*, RagB stimulates the activity of the peptidoglycan polymerase RodA in Bacillus subtilis. *EMBO Rep.* **26**, 4587–4606 (2025).
19. J. Delisle *et al.*, Characterization of TseB: A new actor in cell wall elongation in Bacillus subtilis. *Mol. Microbiol.* **116**, 1099–1112 (2021).
20. N. G. Greene, C. Fumeaux, T. G. Bernhardt, Conserved mechanism of cell-wall synthase regulation revealed by the identification of a new PBP activator in Pseudomonas aeruginosa. *Proc. Natl. Acad. Sci. U.S.A.* **115**, 3150–3155 (2018).
21. C. Midonet *et al.*, MacP bypass variants of Streptococcus pneumoniae PBP2a suggest a conserved mechanism for the activation of bifunctional cell wall synthases. *mBio* **14**, e02390-23 (2023).
22. J. W. Sher, H. C. Lim, T. G. Bernhardt, Global phenotypic profiling identifies a conserved actinobacterial cofactor for a bifunctional PBP-type cell wall synthase. *eLife* **9**, e54761 (2020).
23. T. M. Bartlett *et al.*, FacZ is a GpsB-interacting protein that prevents aberrant division-site placement in Staphylococcus aureus. *Nat. Microbiol.* **9**, 801–813 (2024).
24. A. K. Fenton, L. E. Mortaji, D. T. C. Lau, D. Z. Rudner, T. G. Bernhardt, CozE is a member of the MreCD complex that directs cell elongation in Streptococcus pneumoniae. *Nat. Microbiol.* **2**, 16237 (2016).
25. J. Burnier *et al.*, Pneumococcal S protein coordinates cell wall modification and repair to resist host antimicrobials. *Nat. Microbiol.* **11**, 282–300 (2026).
26. H. Millat *et al.*, Streptococcus pneumoniae S protein activates PBP1a to regulate peptidoglycan remodelling and cell division. *Nat. Microbiol.* **11**, 301–316 (2026).
27. F. Ramos-León *et al.*, PcdA promotes orthogonal division plane selection in Staphylococcus aureus. *Nat. Microbiol.* **9**, 2997–3012 (2024).
28. M. Martinez *et al.*, Eukaryotic-like gephyrin and cognate membrane receptor coordinate corynebacterial cell division and polar elongation. *Nat. Microbiol.* **8**, 1896–1910 (2023).
29. C.-M. Kang, S. Nyayapathy, J.-Y. Lee, J.-W. Suh, R. N. Husson, Wag31, a homologue of the cell division protein DivIVA, regulates growth, morphology and polar cell wall synthesis in mycobacteria. *Microbiology* **154**, 725–735 (2008).
30. P. J. Eswara *et al.*, An essential Staphylococcus aureus cell division protein directly regulates FtsZ dynamics. *eLife* **7**, e38856 (2018).
31. J. Zhang *et al.*, Predicting protein-protein interactions in the human proteome. *Science* **390**, eadt1630 (2025).
32. I. R. Humphreys *et al.*, Protein interactions in human pathogens revealed through deep learning. *Nat. Microbiol.* **9**, 2642–2652 (2024).
33. E. W. Schmid *et al.*, Proteome-wide in silico screening for human protein-protein interactions. bioRxiv [Preprint] (2025). https://doi.org/10.1101/2025.11.10.687652 (Accessed 15 March 2026).
34. Y. Lim *et al.*, In silico protein interaction screening uncovers DONSON's role in replication initiation. *Science* **381**, eadi3448 (2023).
35. B.-M. Koo *et al.*, Comprehensive genetic interaction analysis of the Bacillus subtilis envelope using double-CRISPRi. *Cell Syst.* **16**, 101406 (2025).
36. M. Santiago *et al.*, Genome-wide mutant profiling predicts the mechanism of a Lipid II binding antibiotic. *Nat. Chem. Biol.* **14**, 601–608 (2018).
37. F. H. Ramírez-Guadiana *et al.*, Identification of sporulation genes in Bacillus anthracis highlights similarities and significant differences with Bacillus subtilis. *PLoS Biol.* **23**, e3003521 (2025).
38. J. van Heijenoort, Formation of the glycan chains in the synthesis of bacterial peptidoglycan. *Glycobiology* **11**, 25R–36R (2001).

39. N. T. Reichmann *et al.*, SEDS–bPBP pairs direct lateral and septal peptidoglycan synthesis in Staphylococcus aureus. *Nat. Microbiol.* **4**, 1368–1377 (2019).
40. J.-C. Lee, G. C. Stewart, Essential nature of the mreC determinant of *Bacillus subtilis*. *J. Bacteriol.* **185**, 4490–4498 (2003).
41. S. F. Costa *et al.*, The role of GpsB in *Staphylococcus aureus* cell morphogenesis. *mBio* **15**, e03235-23 (2024).
42. A. O. Henriques, P. Glaser, P. J. Piggot, C. P. Moran Jr., Control of cell shape and elongation by the rodA gene in Bacillus subtilis. *Mol. Microbiol.* **28**, 235–247 (1998).
43. Y. Kawai *et al.*, A widespread family of bacterial cell wall assembly proteins. *EMBO J.* **30**, 4931–4941 (2011).
44. G. Karimova, J. Pidoux, A. Ullmann, D. Ladant, A bacterial two-hybrid system based on a reconstituted signal transduction pathway. *Proc. Natl. Acad. Sci. U.S.A.* **95**, 5752–5756 (1998).
45. E. W. Schmid, J. C. Walter, Predictomes, a classifier-curated database of AlphaFold-modeled protein-protein interactions. *Mol. Cell* **85**, 1216–1232.e5 (2025).
46. W. Zhu, A. Shenoy, P. Kundrotas, A. Elofsson, Evaluation of AlphaFold-Multimer prediction on multi-chain protein complexes. *Bioinformatics* **39**, btad424 (2023).
47. D. B. Clewell, F. Y. An, B. A. White, C. Gawron-Burke, Streptococcus faecalis sex pheromone (cAM373) also produced by Staphylococcus aureus and identification of a conjugative transposon (Tn918). *J. Bacteriol.* **162**, 1212–1220 (1985).
48. K. Schilcher *et al.*, The Staphylococcus aureus CamS lipoprotein is a repressor of toxin production that shapes host-pathogen interaction. *PLoS Biol.* **22**, e3002451 (2024).
49. P. J. Youngman, J. B. Perkins, R. Losick, Genetic transposition and insertional mutagenesis in Bacillus subtilis with Streptococcus faecalis transposon Tn917. *Proc. Natl. Acad. Sci. U.S.A.* **80**, 2305–2309 (1983).
50. S. Herbert *et al.*, Repair of global regulators in Staphylococcus aureus 8325 and comparative analysis with other clinical isolates. *Infect. Immun.* **78**, 2877–2889 (2010).
51. A. J. Meeske *et al.*, High-throughput genetic screens identify a large and diverse collection of new sporulation genes in *Bacillus subtilis*. *PLoS Biol.* **14**, e1002341 (2016).
52. G. S. Dobihal, J. Flores-Kim, I. J. Roney, X. Wang, D. Z. Rudner, The WalR-WalK signaling pathway modulates the activities of both CwlO and LytE through control of the peptidoglycan deacetylase PdaC in Bacillus subtilis. *J. Bacteriol.* **204**, e00533-21 (2021).
53. M. Mirdita *et al.*, ColabFold: Making protein folding accessible to all. *Nat. Methods* **19**, 679–682 (2022).
54. J. Jumper *et al.*, Highly accurate protein structure prediction with AlphaFold. *Nature* **596**, 583–589 (2021).
55. R. Evans *et al.*, Protein complex prediction with AlphaFold-Multimer. bioRxiv [Preprint] (2022). https://doi.org/10.1101/2021.10.04.463034 (Accessed 7 March 2022).
56. M. Steinegger, J. Söding, MMseqs2 enables sensitive protein sequence searching for the analysis of massive data sets. *Nat. Biotechnol.* **35**, 1026–1028 (2017).
57. A. D. Brito *et al.*, mAIcrobe: An open-source framework for high-throughput bacterial image analysis. bioRxiv [Preprint] (2025). https://doi.org/10.1101/2025.10.21.683709 (Accessed 15 March 2026).
58. X. Wang *et al.*, Condensin promotes the juxtaposition of DNA flanking its loading site in Bacillus subtilis. *Genes Dev.* **29**, 1661–1675 (2015).
59. M. Fujita, Y. Sadaie, Promoter selectivity of the Bacillus subtilis RNA polymerase 6k and CTH holoenzyme. *J. Biochem.* **124**, 89–97 (1998).
60. D. H. Parks *et al.*, GTDB release 10: A complete and systematic taxonomy for 715 230 bacterial and 17 245 archaeal genomes. *Nucleic Acids Res.* **54**, D743–D754 (2025).
61. D. Hyatt *et al.*, Prodigal: Prokaryotic gene recognition and translation initiation site identification. *BMC Bioinformatics* **11**, 119 (2010).
62. I. Letunic, P. Bork, Interactive Tree Of Life (iTOL) v5: An online tool for phylogenetic tree display and annotation. *Nucleic Acids Res.* **49**, gkab301 (2021).
63. J. Schindelin *et al.*, Fiji: An open-source platform for biological-image analysis. *Nat. Methods* **9**, 676–682 (2012).
64. P. Thevenaz, U. E. Ruttimann, M. Unser, A pyramid approach to subpixel registration based on intensity. *IEEE Trans. Image Process.* **7**, 27–41 (1998).
65. A. Ducret, E. M. Quardokus, Y. V. Brun, MicrobeJ, a tool for high throughput bacterial cell detection and quantitative analysis. *Nat. Microbiol.* **1**, 16077 (2016).
66. A. P. Brogan, E. W. Schmid, D. Z. Rudner, A broadly conserved Gram-positive lipoprotein regulates cell elongation. NCBI Sequence Read Archive. https://www.ncbi.nlm.nih.gov/bioproject/PRJNA1435919. Deposited 11 March 2026.